Deep-Nanoscale Pattern Engineering by Immersion-Induced Self-Assembly

Woon Ik Park,[†,‡] Jong Min Kim,[†] Jae Won Jeong,[†] and Yeon Sik Jung*[,†]

[†]Department of Materials Science and Engineering, Korea Advanced Institute of Science and Technology (KAIST), 291 Daehak-ro, Yuseong-gu, Daejeon 305-701, Republic of Korea and [‡]R&D Center for Hybrid Interface Materials (HIM), Busandaehak-ro 63beon-gil, Geumjeong-gu, Busan 609-735, Republic of Korea

ABSTRACT The directed self-assembly (DSA) of block copolymers (BCPs) is expected to complement conventional optical lithography due to its excellent pattern resolution and cost-effectiveness. Recent studies have shown that BCPs with a large Flory–Huggins interaction parameter (χ) are critical for a reduction of the thermodynamic defect density as well as an increase in pattern density. However, due to their slower self-assembly kinetics, high-χ BCPs typically necessitate solvent vapor annealing, which requires complex facilities and procedures compared to simple thermal annealing. Here, we introduce an immersion-triggered directed self-assembly (iDSA) process and demonstrate the combined advantages of excellent simplicity, productivity, large-area capability, and tunability. We show that the vapor-free, simple immersion of high-χ BCPs in a composition-optimized mixture of nonswelling and swelling solvents can induce the ultrafast ($\leq$5 min) formation of nanoscale patterns with a pattern size ranging from 8–18 nm. Moreover, iDSA enables the reversible formation of seven different nanostructures from one sphere-forming BCP, demonstrating the outstanding controllability of this self-assembly route.

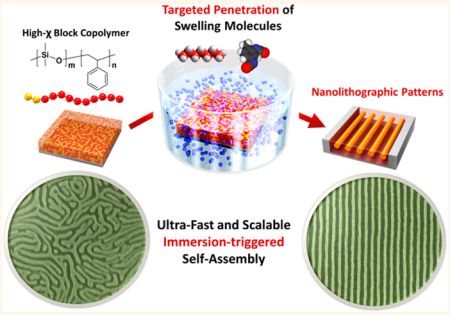

KEYWORDS: immersion · sub-15 nm · polymer · self-assembly · lithography

Directed self-assembly (DSA) based on block copolymers (BCPs) has garnered much attention from semiconductor industries because self-organized BCP patterns have shown excellent ordering characteristics in the size range of 5–50 nm.[1−14] Recent key accomplishments include the successful combination of traditional ArF lithography with DSA and its implementation on 300 mm wafers.[15−18] Currently, a further reduction of the pattern size (*e.g.*, sub-10 nm half-pitch patterns) and the achievement of a uniform alignment using a BCP with a high Flory–Huggins interaction parameter (χ) are two key directions in the DSA research.[4,10] Moreover, theoretical studies show that the thermodynamic defect density of BCP patterns exponentially scales with χ and that the interfacial width, affecting the line edge roughness, is inversely proportional to χ.[19,20] Along with the achievement of the formation of sub-10 nm patterns, these combined advantages of high-χ BCPs have already been reported in previous studies.[4−6,9,10,19−25]

However, the chain mobility of BCPs decreases exponentially with the segregation strength (χN), the product of χ and the degree of polymerization (N),[26] resulting in a much lower throughput during the pattern formation process. Moreover, conventional thermal annealing often produces only nonequilibrium, kinetically trapped morphologies and fails to induce the formation of high-quality patterns from a high-χ BCP.[27] In contrast, the long-range ordering of high-χ BCPs has been successfully achieved using solvent vapor treatments.[6,9,14,21,27,28] which can effectively plasticize polymer chains. Moreover, the outstanding controllability in orientation and pattern geometry has also been suggested as an additional benefit.[6,21,27,28] Recently, the ultrafast formation (an assembly time less than a few minutes) of self-assembled patterns was demonstrated using solvothermal treatments by a synergic enhancement effect on the polymer chain mobility both by solvent plasticization and thermal activation.[29,30] However, compared to the simplicity of thermal annealing, it has been questioned whether solvent vapor annealing is compatible with general semiconductor manufacturing.[4,10] One factor which increases the complexity of solvent vapor annealing is that the vapor should be

* Address correspondence to ysjung@kaist.ac.kr.

Received for review April 15, 2014 and accepted October 7, 2014.

Published online October 10, 2014
10.1021/nn504995c

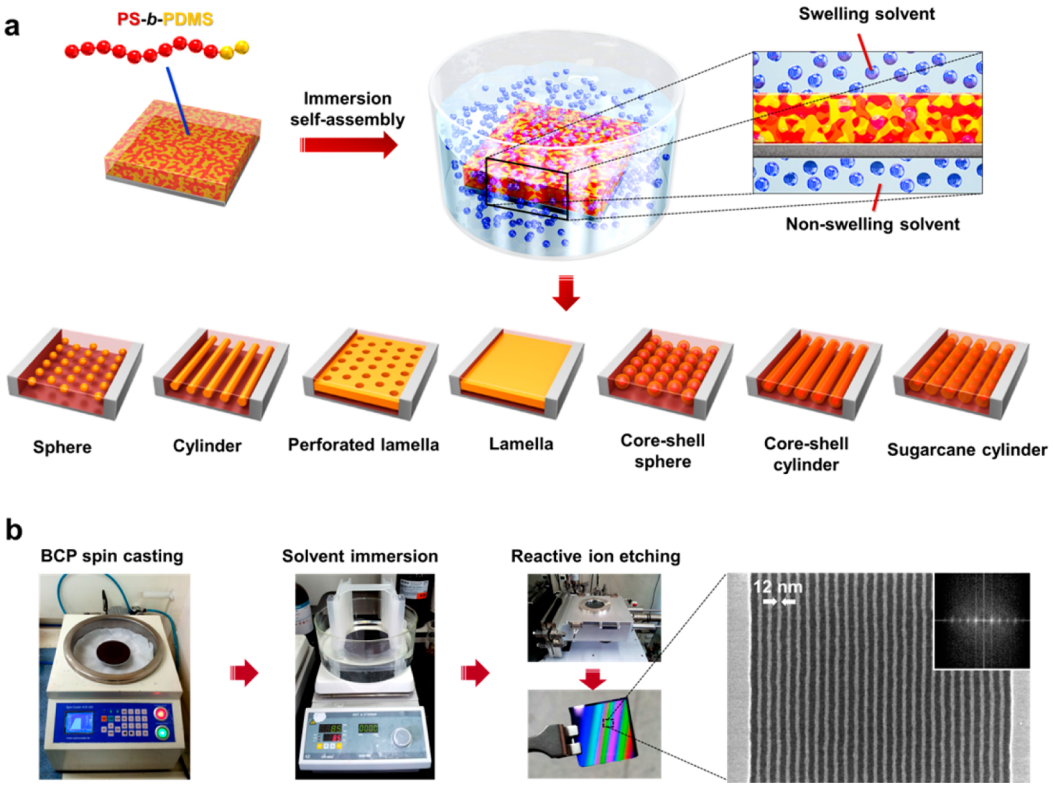

Figure 1. Concept of immersion-triggered self-assembly (iDSA). (a) Schematic of iDSA. A BCP film is immersed into the mixture of swelling and nonswelling solvents. The swelling solvent molecules penetrate into the BCP film and induce the self-assembly process. Various self-assembly nanostructures, such as spheres, cylinders, perforated lamella, lamellae, core−shell spheres, core−shell cylinders, and sugar cane cylinders can be formed from one BCP (PS-*b*-PDMS, SD51). (b) Procedure of the iDSA method, consisting of BCP spin-casting, immersion in the solvent mixture, and reactive ion etching to remove the PS and to oxidize the PDMS. The SEM image shows line and space patterns prepared from the SD51 BCP using iDSA.

generated from a liquid source and then efficiently and evenly delivered to the entire wafer surface to ensure the uniform swelling of BCP thin films. This requires the use of an efficient vapor generation process and a reliable delivery system compatible with CMOS fabrication technologies. Such system with a large-area assembly capability has not yet been developed or demonstrated, to the best of our knowledge, due to the inevitable complexity associated with the handling of solvent vapors.

Here, we present immersion-triggered directed self-assembly (iDSA) method to simplify, expedite, and control the self-assembly of high-χ BCPs and, accordingly, to form 8−18 nm patterns. We report that BCP films immersed in a blend of swelling and nonswelling solvents can be extensively controlled and appropriately swollen by the targeted penetration of swelling solvents as schematically shown in Figure 1a. This extremely simple approach resembles the typical photoresist development process in photolithography, which is widely used for the selective removal of soluble components in UV-exposed photoresist films, suggesting the excellent compatibility with CMOS fabrication process. Moreover, we demonstrate that iDSA can provide greatly extended tunability in self-assembled geometries. Using one BCP to form dot patterns when thermally annealed, we show how to obtain several different morphologies: sphere, cylinder, hexagonally perforated lamella, lamella, core−shell sphere, core−shell cylinder, and sugar cane cylinder.

RESULTS AND DISCUSSION

For the demonstration of the iDSA method, we chose poly(styrene-*b*-dimethylsiloxane) (PS-*b*-PDMS) as a model system for high-χ BCPs with a known χ parameter of 0.26 at room temperature,[6] which is at least several times larger than that of poly(styrene-*b*-methyl methacrylate) (PS-*b*-PMMA).[31] The preferential existence of Si in the PDMS block provides a high degree of etch selectivity (>10:1) between the two constituent polymer blocks under O_2 plasma etching conditions, easily revealing the oxidized PDMS nanopatterns for the subsequent pattern transfer and characterization. As a nonswelling solvent for PS-*b*-PDMS, where both of the blocks are hydrophobic, a polar solvent (ethanol) was chosen because its Hildebrand solubility parameter ($\delta \sim 26.2$ MPa$^{1/2}$) is sufficiently different from those of PS ($\delta \sim 18.5$ MPa$^{1/2}$) and PDMS ($\delta \sim 15.5$ MPa$^{1/2}$).[32] As a result, the immersion of PS-*b*-PDMS BCPs in pure ethanol (a fraction of toluene, $f_{TOL} = 0$) did not cause the swelling of the BCP film or any morphological change from the as-spun sample

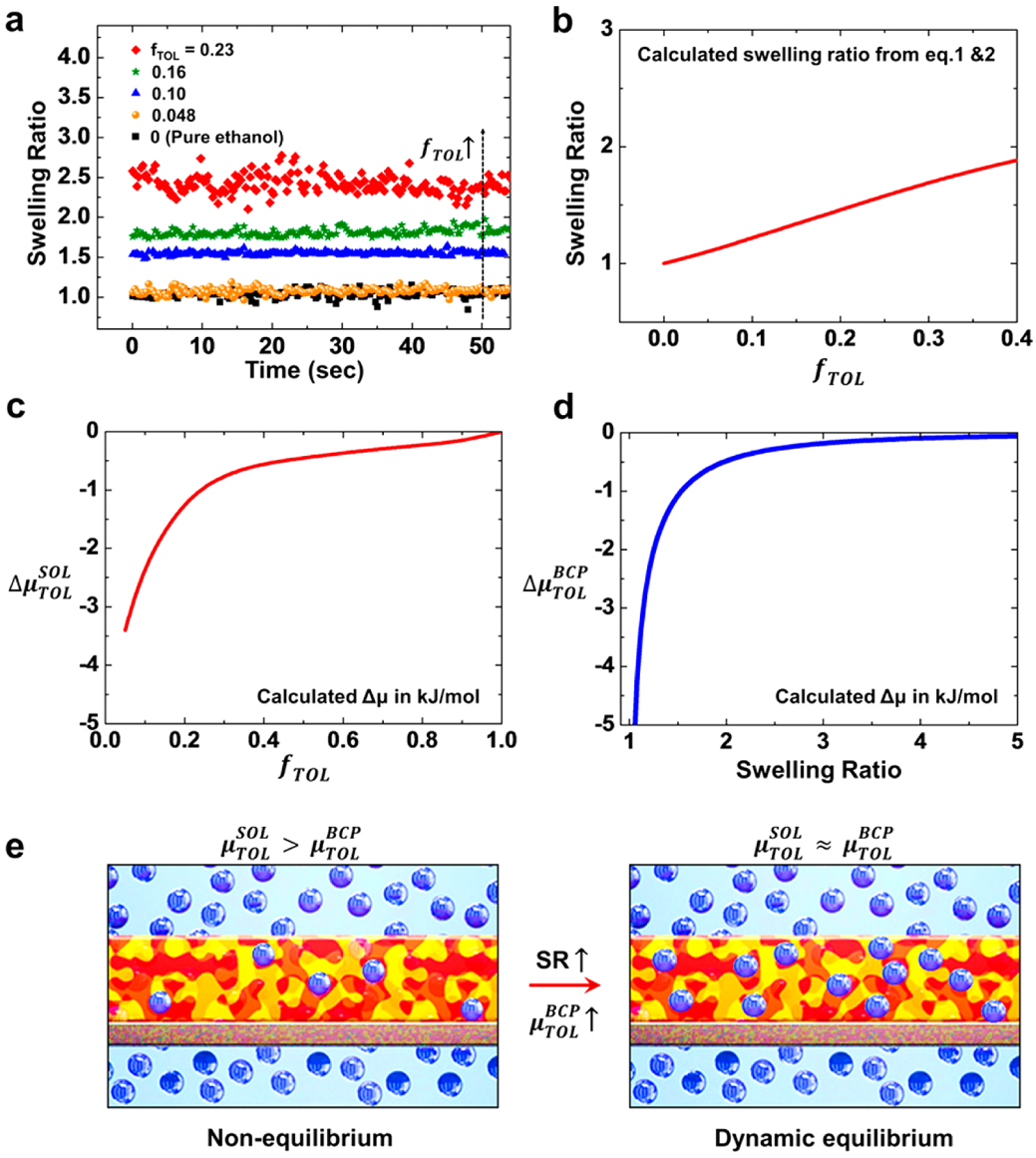

Figure 2. Control of the BCP swelling ratio (SR) by solvent immersion. (a) Measured SR of a PS-*b*-PDMS BCP thin film immersed in a mixture of swelling (toluene) and nonswelling (ethanol) solvents with different f_{TOL} values. Here, $t = 0$ s does not indicate the starting point of swelling. Because of the fast swelling dynamics of the BCP films in the heated solvent mixture, the samples arrived at the saturated SR within the measurement preparation time. Thus, $t = 0$ indicates the initiation point of measurement after the saturation of SR. (b) Calculated equilibrium SR depending on f_{TOL}. (c,d) Calculated chemical potentials of toluene (c) in the solvent mixture as a function of f_{TOL} and (d) in the solvent-swollen BCP as a function of SR. (e) Illustrations of different swelling states and a comparison of the chemical potentials.

(Figure 2a and Figure S1 in the Supporting Information). This tendency was consistent for all the BCPs with different molecular weights (MWs) ranging from 16 to 51 kg/mol (Figure S1). Methanol with a δ value of ~29.7 $MPa^{1/2}$ also did not cause any noticeable difference in the thin-film morphologies, suggesting that various polar solvents (with a sufficiently large δ values such that they will not swell the any of the polymer blocks) would be viable candidates for a nonswelling solvent. On the other hand, the δ value of a nonswelling solvent should not be too large, as good miscibility with a swelling solvent (*e.g.*, toluene) should be ensured. Alcoholic solvents (*e.g.*, ethanol or methanol) satisfy these requirements well enough.

In contrast, an appropriate addition of a swelling solvent (toluene) to the nonswelling solvent effectively induces the swelling of the BCP film, as shown in Figure 2a. For example, a swelling ratio (SR = the swollen thickness divided by the dry thickness) of ~2.5 was obtained at a f_{TOL} (the mole fraction of toluene in the toluene/ethanol mixture) value of 0.23. The estimation of SR is important for the understanding of the self-assembly behavior of BCP microdomains.[33] The swelling ratio values measured *in situ* using thin film reflectometry (see Figure S2 for measurement configurations) show stable averages depending on f_{TOL}. Immediately after the immersion treatment of the BCP films, the samples were rinsed in ethanol for 10 s

and dried by N_2 blowing in order to remove remaining solvent from the BCP film surface. The fluctuation of *in situ* measured swelling ratio is thought to be related to the liquid nature of the medium. The oscillation of the liquid surface level can refract the reflected beams on the BCP sample surface and interfere with the collection of reflected light through the fiber optic. Thus, we used the averaged values (from more than 150 data points) to estimate the swelling ratio of the samples under different immersion conditions. Although the swelling ratio profile during the final drying process could not be *in situ* monitored, the thickness of the BCP film was *ex-situ* measured using the same reflectometry system. It was confirmed that the BCP film thickness immediately after the drying process was restored to the original dry thickness (34−35 nm), as shown in Figure S3, indicating that all the solvent was completely removed.

Figure 2a clearly shows the rise of SR with an increase in f_{TOL}. This phenomenon can be explained by an analytical model based on thermodynamic theories of solvents and polymer solutions. First, from the regular solution model, the difference between the chemical potential (μ_{TOL}^{sol}) of toluene molecules in the toluene/ethanol mixture and that (μ_{TOL}^{o}) of the molecules in pure liquid toluene is associated with the mixing free energy of the two solvents.

$$\Delta\mu_{TOL} = \mu_{TOL}^{sol} - \mu_{TOL}^{o} = RT \ln(\gamma_{TOL} f_{TOL}) \quad (1)$$

where γ_{TOL} is the activation coefficient of toluene in the mixture, R is the gas constant, and T is the solution temperature. By referring to previously reported γ_{TOL} values,[34] eq 1 as a function of f_{TOL} is plotted in Figure 2c. Also, using Flory−Huggins theories, the chemical potential difference ($\Delta\mu_{TOL} = \mu_{TOL}^{BCP} - \mu_{TOL}^{o}$) between toluene molecules in the BCP/toluene mixture and in a pure liquid can be calculated, as follows:

$$\Delta\mu_{TOL} = \mu_{TOL}^{BCP} - \mu_{TOL}^{o} = RT[\ln(1 - \phi_{BCP}) + \phi_{BCP} + \chi_{TOL-BCP}\phi_{BCP}^{2}] \quad (2)$$

In this equation, $\chi_{TOL-BCP}$ is the effective interaction parameter between toluene and BCP, and ϕ_{BCP} (= 1/SR) is the volume fraction of BCP in the solvent-swollen BCP. The increasing tendency of μ_{TOL}^{BCP} as a function of SR is shown in Figure 2d. While μ_{TOL}^{mix} is simply determined by the mixing ratio of toluene and ethanol, the solvent-immersion of BCP gradually increases μ_{TOL}^{BCP} as more toluene molecules infiltrate into the BCP film until μ_{TOL}^{BCP} reaches the value of μ_{TOL}^{sol} as schematically illustrated by Figure 2e. We can assume that f_{TOL} does not change during the BCP swelling process because the quantity of toluene incorporated into the BCP film is negligible compared to the amount of toluene in the immersion solution considering the thin thickness (25−35 nm) of BCP thin films. In the thermodynamic equilibrium swelling state, the chemical potential (μ_{TOL}^{BCP}) of toluene in the swollen BCP will be equal to that (μ_{TOL}^{sol}) in the solvent mixture. Thus, the condition of $\mu_{TOL}^{sol} = \mu_{TOL}^{BCP}$ indicates that eq 1 = eq 2, whose solution provides the calculated equilibrium SR values shown in Figure 2b, demonstrating the increasing tendency in the equilibrium SR with f_{TOL}. This thermodynamic model demonstrates that a careful selection of the mixing ratio provides the ability to control the SR of BCP films as the experimental data in Figure 2a confirm. From this clear relationship, the SR values can easily be identified without measuring it for all the samples. The curve of experimentally measured SR *vs* f_{TOL} is plotted and shown in Figure S4, enabling the fast and convenient estimation of SR as a function of f_{TOL} by relaying on the clear dependence of SR on f_{TOL}. The higher measured SR values of the BCP thin films than the calculated ones from the model can be explained by the effect that the structural frustration and the consequential loss of conformational entropy of polymer chains at interfaces (*e.g.*, polymer−air and polymer−substrate interfaces) additionally contribute to the increase of the equilibrium SR for thin polymer films under the same environment.[35]

We explored how the controlled SR affects the self-assembly behavior of the PS-*b*-PDMS BCPs with a MW of 51.5 kg/mol (SD51) and a PDMS volume fraction (f_{PDMS}) of 17.5% and with a 45.5 kg/mol (SD45, f_{PDMS} = 34.5%). As shown in Figure 3a and Figure S5, the obtained morphologies were highly dependent on the key treatment parameters of f_{TOL}, the immersion temperature (T), and the immersion time (t). Figures 3a present the changes in the morphologies of SD51 as a function of f_{TOL} and t while fixing T at 85 °C. When the f_{TOL} value was small (≤0.16), the immersion treatment produced spherical patterns, which appear to be similar to the as-spun samples, although the size uniformity and degree of ordering are evidently improved by the immersion annealing process. However, the increase of f_{TOL} to ∼0.23 enabled the formation of 12 nm-wide line patterns (the first morphological transition, sphere-to-cylinder). An immersion treatment of the BCP for 5 min provided uniform ordering in 1-μm-wide trenches, as shown in Figure 3b (middle-left). A further increase of f_{TOL} produced dot patterns for short annealing times ($t \sim 1$ min) and caused dewetting eventually for a longer t in the case of too large SR, causing the instability of the BCP thin films. The stability of the BCP film was highly dependent on f_{TOL}. While the stability time (>100 min) for the optimal f_{TOL} of 0.15 is much longer than the required assembly time (∼5 min) to achieve high-quality patterns, the BCP film rapidly dissolved into the solvent in 5 min for a high f_{TOL} of 0.31. Figure S6 shows the film stability time of the SD51 BCP film as a function of f_{TOL} on the basis of SEM observations. However, with appropriate processing conditions (*e.g.*, f_{TOL} = 0.23), the stability of the BCP

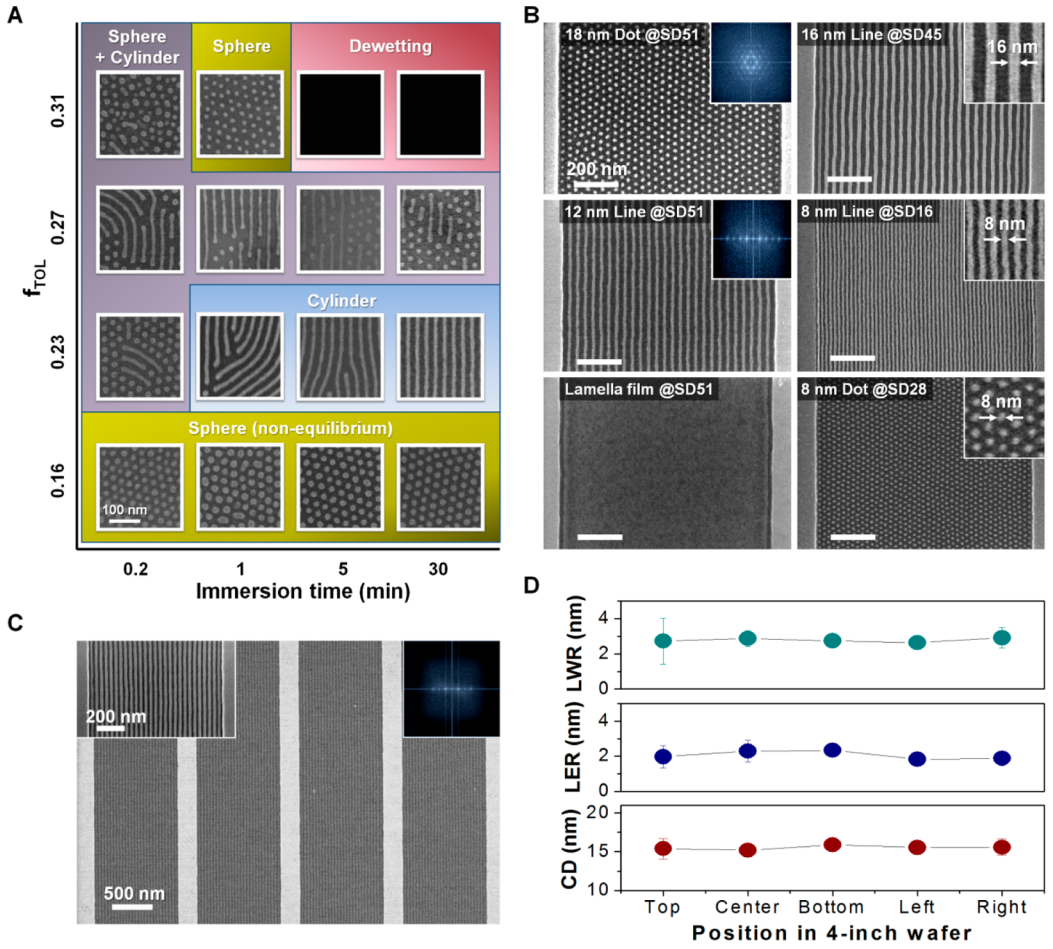

Figure 3. Demonstration of iDSA. (a) Self-assembled morphologies of the SD51 (PS-*b*-PDMS, MW = 51 kg/mol) BCP treated with different solvent compositions (f_{TOL}) and immersion times (t). Under proper swelling conditions, well-aligned nanopatterns can be obtained. (b) Well-ordered dot, line, and lamellar patterns with different feature sizes obtained from various PS-*b*-PDMS BCPs with different molecular weights and minority volume fractions. (c) A low-magnification SEM image of the SD45 BCP assembled by iDSA. (d) Variations of the critical dimension (CD), line edge roughness (LER), and line width roughness (LWR) depending on the chip position on a 4-in wafer.

films was maintained and confirmed by the constant film morphology, as investigated with optical microscopy and SEM imaging (Figure S7).

The second morphological transition (cylinder-to-sphere) can be understood in terms of the fact that the minority volume fraction (f_{PDMS} = 17.5%) of the SD51 BCP in a dry state is close to the boundary region between the cylindrical and spherical phases of the BCP. Thus, the relatively small degree of preferential swelling for PS with a lower value of f_{TOL} (~0.23) can lead to the formation of a cylindrical morphology, while a higher degree of swelling in the PS block with a larger f_{TOL} (~0.31) decreases the effective f_{PDMS} in a highly solvent-swollen BCP, consequently causing the formation of spherical patterns. The occurrence of spherical domains at a much smaller f_{TOL} (~0.16) value can be explained by the fact that untreated SD51 samples cast from a toluene solution show spherical microdomains (Figure S1) due to the preferential affinity between the PS block and the toluene. The slight rearrangement of the polymer chains under limited chain mobility due to the low BCP SR at a small f_{TOL} is thought to result in the formation of those ordered (nonequilibrium) dot patterns. (Figure 3b, top-left)

The immersion temperature T also significantly affected the self-assembly kinetics. When the PS-*b*-PDMS with a MW of 45 kg/mol (SD45) film was immersed in the mixture of toluene and ethanol (f_{TOL} = 0.23) at room temperature (25 °C), it took 8 h to obtain a well-ordered line pattern (Figure S5). However, a good alignment of microdomains was obtained in less than 5 min with the same f_{TOL} value by increasing the immersion temperature to 85 °C (Figure S5). The defect density (D) can be expressed using the formula $D \sim t^{-n}$. The empirical time-decay exponents (n) for T values of 25 and 85 °C were estimated to be 0.69 and 2.7, respectively, showing a much faster annihilation of defects at the higher T. Furthermore, despite the relatively slower kinetics of high-χ BCPs, the high n value of 2.7 at 85 °C suggests that the defect decay of iDSA is significantly faster than that of conventional thermal annealing of low-χ PS-*b*-PMMA.[36]

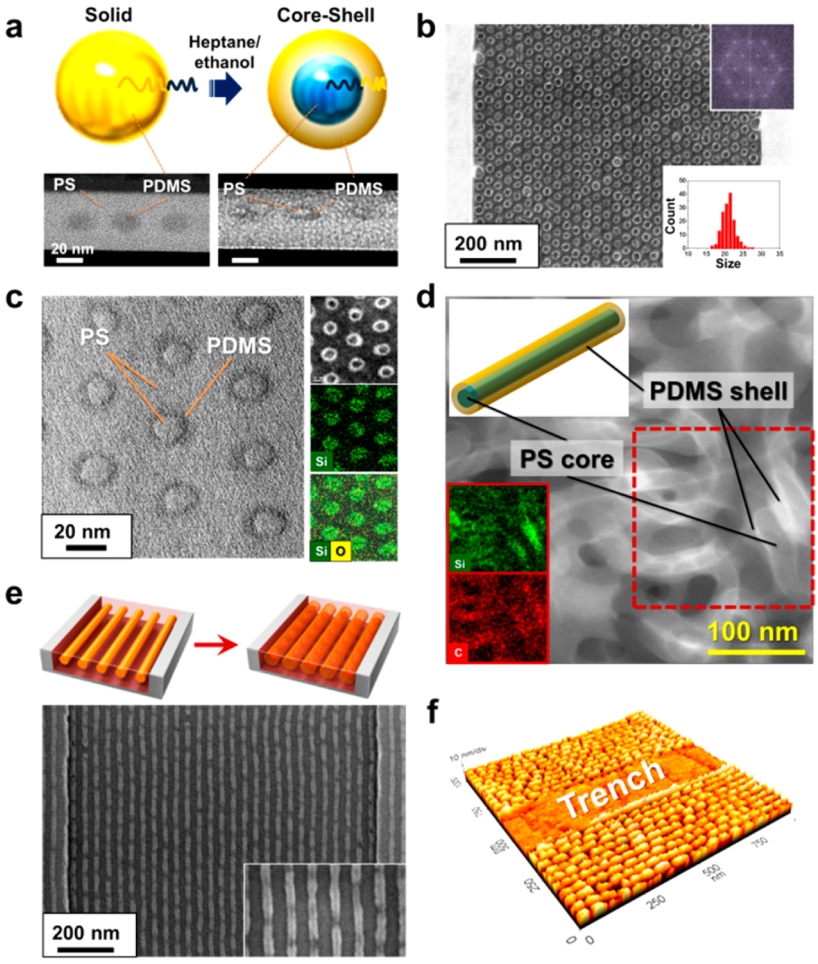

Figure 4. Two-step immersion self-assembly for the alignment of core–shell nanostructures. (a) Cross-sectional TEM images of self-assembled PDMS spheres (bottom-left) annealed at f_{TOL} = 0.10 (first immersion) and core (PS)-shell (PDMS) nanoparticles (bottom-right) produced by the subsequent second immersion treatment at f_{HEP} = 0.056. (b) SEM image and size distribution of the core–shell particles. (c) TEM analysis of the core–shell nanoparticles. Bright-field (left) and dark-field (right-top) images clearly show the formation of core–shell particles, as supported by the EDS elemental mapping of Si and O (right-middle and right-bottom). (d) TEM images of a core–shell cylinder nanostructure. The second treatment was done at f_{HEP} = 0.26. (e) SEM and (f) AFM images of a sugar cane nanostructure, showing good alignment in a topographic template.

Figure 3b shows that the iDSA method is effective for BCPs with a wide MW range; 45 kg/mol (SD45, f_{PDMS} = 34.5%), 16 kg/mol (SD16, f_{PDMS} = 33.1%), and 28 kg/mol (SD28, f_{PDMS} = 11.5%), demonstrating well-ordered lines with widths of 16 and 8 nm and dots with diameters of 8 nm, respectively. Table S1 in the Supporting Information presents the geometry, CD, and CD uniformity data of several iDSA patterns obtained with different BCPs and f_{TOL}, demonstrating the controllability range of iDSA. Table S2 also shows that immersion time has a negligible effect on the CD, CDU, and pitch of the DSA patterns, respectively, within the stability time. These data and the immersion time range shown in Figure S6 provide the process window of iDSA. Furthermore, the possibility of the wafer-level scaling-up of iDSA was investigated by attaching small chip samples onto a four-inch wafer and performing iDSA, as shown in Figure 3d, demonstrating the good uniformity of the critical dimension (CD), the 3σ line edge roughness (LER), and the 3σ line width roughness (LWR). The standard deviations of CD, 3σ LER, and 3σ LWR were estimated to be 0.262, 0.115, and 0.239 nm, respectively.

Similarly, Figure S8 shows that the mixed solvent of heptane (a preferential solvent for the minority block, PDMS) and ethanol (a nonswelling solvent) also enabled the formation of various morphologies, including solid sphere, perforated lamella, lamella, core–shell sphere, and core–shell cylinder structures, which are distinct from the morphologies obtained for the same BCP (SD51) exposed to toluene and ethanol mixtures that swelled the majority PS block. This result can be attributed to two factors: (1) the increase of f_{PDMS} caused by the selective incorporation of heptane into the PDMS block and (2) the formation of several unique morphologies due to the highly selective nature of the solvent mixture at the polymer–solvent interface. Considering that typical solvent vapor annealing on the same BCP was able to induce the formation of only spherical or cylindrical morphologies, as shown in Figure S9, far greater morphological

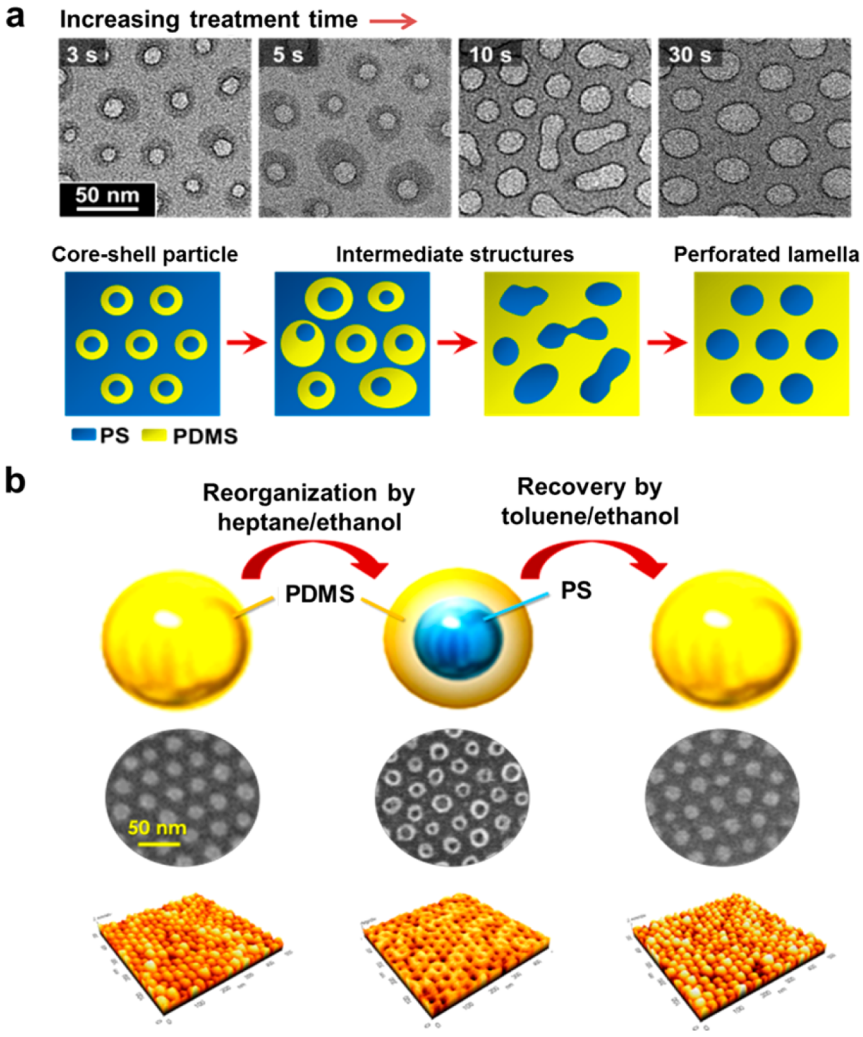

Figure 5. Full reversibility of immersion self-assembly. (a) (top) Time-trace of the reorganization process (second immersion in the mixture of heptane and ethanol) from a solid PDMS sphere to a core–shell particle and to a perforated lamellar structure for monolayered SD51 BCP thin film. (bottom) Schematic illustrations of the morphological transition from the core–shell particle to the perforated lamella structure. (b) Reversible recovery from the core–shell structure to the solid sphere morphology *via* the third immersion treatment using the solvent mixture of toluene and ethanol. The SEM and AFM images show the morphological transformation process from the first original spheres (left, f_{TOL} = 0.23) to the core–shell nanoparticles (middle, f_{HEP} = 0.056), and to the recovered spheres (right, f_{TOL} = 0.23).

diversity and tunability was observed when the solvent immersion annealing process was utilized.

We now demonstrate that a two-step immersion treatment can induce well-ordered core–shell nanostructures. Although a single-step treatment in the same solvent mixture of heptane and ethanol on BCP film can also produce core–shell structures (Figure S8), the degree of ordering and the regularity of the size and shape are relatively poor, most likely due to the limited chain mobility of the majority polymer block (PS, $T_g \sim 100$ °C) in the presence of its nonswelling solvent (heptane). In contrast, well-ordered dot arrays (Figure 3b, top-left) in a 1-μm-wide trench obtained by the treatment in the mixed solvent of toluene and ethanol can be readily converted into core (PS)-shell (PDMS) spheres *via* a simple and short annealing process in the mixture of heptane and ethanol (f_{HEP} = 0.056) while preserving the degree of ordering and good registration in the guiding template, as presented in Figure 4b. The comparison of cross-section transmission electron microscopy (TEM) images of solid PDMS spheres (Figure 4a (left) and Figure S10) *vs* core–shell spheres (Figure 4a (right)) as well as the top-view TEM analysis results presented in Figure 4c and Figure S11 clearly support the formation of the well-defined nanoparticles composed of a PS core and PDMS shell embedded in the PS matrix. The PDMS block appears to be darker in the bright-field image due to the existence of Si. We can differentiate the core–shell nanospheres from conventional micelles as the cross-section TEM image shows that the embedded core–shell spheres are located in the middle of the PS matrix and because the BCP film surface does not show topographical variations before the removal of the PS matrix. Furthermore, they are different from a nanoporous BCP film obtained by reconstruction of

aligned BCP microdomains[37,38] in that our core–shell nanostructures are embedded in continuous BCP films as SEM and AFM images in Figure S12 demonstrate. The porous morphology shown in Figure 4b was obtained only by treating the core–shell morphology with O_2 plasma to remove the central PS and matrix PS domains.

When the BCP films are immersed in the solvent of $f_{HEP} = 0.26$ for 2 s, core (PS)-shell (PDMS) nanowires can also be formed. The energy-dispersive X-ray spectroscopy (EDS) elemental mapping of carbon (C) suggests that the inner domain in the PDMS shell is composed of PS, as shown in the bottom inset of Figure 4d. Supporting TEM analysis and elemental mapping results are also provided in Figure S13. Similarly, as shown in Figure 4e, unusual sugar cane-like nanostructures were obtained when the uniformly aligned cylindrical microdomains (Figure 3b, middle-left) produced by immersion into the mixture of toluene and ethanol were later exposed to the mixture of heptane and ethanol ($f_{HEP} = 0.056$). The magnified image shown in the inset of Figure 4e and the atomic force microscopy (AFM) image shown in Figure 4f reveal the periodic wiggling of the nanowire occurring due to the presence of PS-particulate cores inside the PDMS nanowires. This two-step iDSA using various solvent mixtures with different levels of affinity to polymer blocks can be an effective and simple route to prepare atypical self-assembly nanostructures that are differentiated from the usual spherical or cylindrical morphologies while also providing controllability of their locations and orientations.

We also observed a multistep morphological transformation while monitoring the time-dependent morphological evolution with a further increase in the second immersion treatment time under the condition of $f_{HEP} = 0.056$. Figure 5a shows that the core–shell spheres are progressively converted into the perforated lamella morphology as the treatment duration time increases. During the conversion process, the increase of the PDMS area fraction in the TEM images suggests a gradual expansion of the PDMS block. For the sample treated for 10 s, the expanded PDMS block was observed to be connected, leading to the formation of a continuous PDMS layer containing perforations filled with PS chains, suggesting the metastability of the core–shell spheres under the treatment condition. With a longer treatment time, the PS perforations became more regular and their local ordering was achieved. Moreover, the core–shell spheres reorganized from the spherical morphology can easily be recovered to the original solid spheres *via* an additional treatment using a mixture of toluene and ethanol ($f_{TOL} = 0.23$) (Figure 5b). These results support the outstanding controllability, reversibility, and versatility of the controlled solvent immersion treatment.

CONCLUSIONS

To summarize, we demonstrated that the vapor-free immersion treatment (iDSA) in a solvent mixture composed of swelling and nonswelling solvents can successfully facilitate the self-assembly of BCPs for fast and convenient pattern formation in the sub-20 nm regime. The careful control of solvent composition and other parameters provided well-aligned line and dot patterns with dimensions in the range of 8–18 nm. The outstanding simplicity of iDSA stems from the fact that swelling solvent molecules are directly injected from the liquid source into BCP films without the need to generate vapors. Thermodynamic models substantiate that the equilibrium swelling ratio of the polymer films is determined by the solvent composition, as shown in our experimental observations. We also demonstrated that various types of BCP microdomain morphologies, including unusual core–shell structures, can be obtained by employing a different swelling solvent that penetrated into the minority BCP block. The controlled alignment of the core–shell structures can be achieved by a two-step immersion assembly process consisting of a guided ordering process of spherical or cylindrical structures *via* the first immersion treatment to target the swelling of the majority block and a subsequent second immersion process for conversion into core–shell nanostructures with good registration in topographic templates.

Because of the obvious advantages of outstanding simplicity and effectiveness, we expect that the iDSA process has the potential to replace the conventional solvent-vapor-based annealing method. Moreover, this method may be widely applicable beyond the self-assembly of BCPs to a range of other application areas, such as organic solar cells or nanocrystal self-organization, where a simpler and faster treatment based on solvents can be greatly advantageous.

METHODS

Immersion Self-Assembly of BCP. All BCPs and end-functionalized polymers used in this study were purchased from Polymer Source Inc. (Canada). The Si trench templates with a width of 1 μm and a depth of 40 nm (Figure S14) for iDSA were fabricated using KrF photolithography and reactive ion etching (RIE). To promote self-assembly of BCPs and improve the pattern quality by mitigating the strong interaction between BCP chains and native oxide surface, the Si substrates were functionalized with a hydroxyl-terminated homopolymer (PS–OH, MW = 42 kg/mol) at 150 °C for 2 h in a vacuum oven and washed with toluene to remove any unreacted polymer residues. BCP solutions dissolved in toluene at 1.1 wt % were spin-coated onto the substrates, having a film thickness of ~35 nm, and then immersed in the mixtures of toluene/ethanol or heptane/ethanol in a stainless steel chamber at a temperature of RT–85 °C. The homogeneous mixing of the solvents should be assured for the uniformity of the self-assembly process.

Film Thickness Measurement. The thickness of dry and solvent-swollen BCP films was measured using a thin film reflectometry system (F20−UV, FILMETRICS Inc., USA). For the dry thickness measurement, light reflected from the air/BCP and BCP/Si interfaces is collected, having the reflection coefficients (r_0 and r_1) at 90° from the first (air/BCP) and second (BCP/Si) interfaces, respectively, as follows.

$$r_0 = \frac{n_0 - n_1}{n_0 + n_1} \tag{3}$$

$$r_1 = \frac{n_1 - n_2}{n_1 + n_2} \tag{4}$$

where n_0, n_1, and n_2 are the refractive indices of air, the BCP film, and the Si substrate, respectively.

$$R = |r_0|^2 + |r_1|^2 + 2|r_0||r_1| \cos\frac{2\pi n_1 d}{\lambda} \tag{5}$$

where R, d, and λ are reflectance, BCP film thickness, and wavelength, respectively. R is measured in the λ range of 380−1050 nm, showing a cosine dependence as a function of $1/\lambda$. The BCP film thickness was obtained by finding the n_1 and d values that provide the best value of goodness of fit (GOF) for the measured and calculated reflection spectrum $R(\lambda)$. For the measurement of solvent swollen thickness, a layer stacking model of air/solvent/BCP/native oxide/Si and the same calculation principle was used.

Morphology Characterization. The self-assembled PS-*b*-PDMS microdomains were observed using transmission electron microscopy (TEM) with an energy-dispersive X-ray spectroscopy (EDS). Top-view and cross-sectional transmission electron microscopy (TEM) samples were prepared by mechanical polishing, followed by ion milling with Ar ions. High-resolution TEM (HRTEM) studies were performed using a JEOL JEM-ARM200F microscope operated at 200 kV. All the TEM samples were observed without reactive ion etching (RIE) or staining because of the inherent high contrast between PS and PDMS microdomains. The self-assembled nanostructures were investigated using field emission scanning electron microscopy (FE-SEM: Hitachi S-4800) operated with an acceleration voltage of 10 kV, emission current of 10 μA, and a working distance of 5 mm. The surface topography and roughness of the samples were analyzed using an atomic force microscope (AFM: Park System XE-100) equipped with a Si AFM tip (height/radius: 3 μm/30 nm). All scanning processes were performed at room temperature and ambient pressure.

Conflict of Interest: The authors declare no competing financial interest.

Acknowledgment. This research was supported by Global Frontier Program through the Global Frontier Hybrid Interface Materials (GFHIM) of the National Research Foundation of Korea (NRF) funded by the Ministry of Science, ICT & Future Planning (2013M3A6B1078874).

Supporting Information Available: Additional pattern quality analysis data, morphological changes of BCPs under various iDSA treatment conditions, and TEM/EDS analysis data are included. This material is available free of charge *via* the Internet at http://pubs.acs.org.

REFERENCES AND NOTES

1. Segalman, R. A.; Yokoyama, H.; Kramer, E. J. Graphoepitaxy of Spherical Domain Block Copolymer Films. *Adv. Mater.* **2001**, *13*, 1152–1155.
2. Kim, S. O.; Solak, H. H.; Stoykovich, M. P.; Ferrier, N. J.; de Pablo, J. J.; Nealey, P. F. Epitaxial Self-assembly of Block Copolymers on Lithographically Defined Nanopatterned Substrates. *Nature* **2003**, *424*, 411–414.
3. Cheng, J. Y.; Mayes, A. M.; Ross, C. A. Nanostructure Engineering by Templated Self-Assembly of Block Copolymers. *Nat. Mater.* **2004**, *3*, 823–828.
4. Black, C. T.; Ruiz, R.; Breyta, G.; Cheng, J. Y.; Colburn, M. E.; Guarini, K. W.; Kim, H. C.; Zhang, Y. Polymer Self-assembly in Semiconductor Microelectronics. *IBM J. Res. Dev.* **2007**, *51*, 605–633.
5. Darling, S. B. Directing the Self-Assembly of Block Copolymers. *Prog. Polym. Sci.* **2007**, *32*, 1152–1204.
6. Jung, Y. S.; Ross, C. A. Orientation-Controlled Self-Assembled Nanolithography Using a Polystyrene-Polydimethylsiloxane Block Copolymer. *Nano Lett.* **2007**, *7*, 2046–2050.
7. Bita, I.; Yang, J. K.; Jung, Y. S.; Ross, C. A.; Thomas, E. L.; Berggren, K. K. Graphoepitaxy of Self-Assembled Block Copolymers on Two-Dimensional Periodic Patterned Templates. *Science* **2008**, *321*, 939–943.
8. Ruiz, R.; Kang, H. M.; Detcheverry, F. A.; Dobisz, E.; Kercher, D. S.; Albrecht, T. R.; de Pablo, J. J.; Nealey, P. F. Density Multiplication and Improved Lithography by Directed Block Copolymer Assembly. *Science* **2008**, *321*, 936–939.
9. Park, S.; Lee, D. H.; Xu, J.; Kim, B.; Hong, S. W.; Jeong, U.; Xu, T.; Russell, T. P. Macroscopic 10-Terabit-per-Square- Inch Arrays from Block Copolymers with Lateral Order. *Science* **2009**, *323*, 1030–1033.
10. Bates, C. M.; Seshimo, T.; Maher, M. J.; Durand, W. J.; Cushen, J. D.; Dean, L. M.; Blachut, G.; Ellison, C. J.; Willson, C. G. Polarity-Switching Top Coats Enable Orientation of Sub-10-nm Block Copolymer Domains. *Science* **2012**, *338*, 775–779.
11. Stoykovich, M. P.; Muller, M.; Kim, S. O.; Solak, H. H.; Edwards, E. W.; de Pablo, J. J.; Nealey, P. F. Directed Assembly of Block Copolymer Blends into Nonregular Device-Oriented Structures. *Science* **2005**, *308*, 1442–1446.
12. Tang, C. B.; Lennon, E. M.; Fredrickson, G. H.; Kramer, E. J.; Hawker, C. J. Evolution of Block Copolymer Lithography to Highly Ordered Square Arrays. *Science* **2008**, *322*, 429–432.
13. Yang, J. K. W.; Jung, Y. S.; Chang, J. B.; Mickiewicz, R. A.; Alexander-Katz, A.; Ross, C. A.; Berggren, K. K. Complex Self-Assembled Patterns Using Sparse Commensurate Templates with Locally Varying Motifs. *Nat. Nanotechnol* **2010**, *5*, 256–260.
14. Tavakkoli, K. G. A.; Gotrik, K. W.; Hannon, A. F.; Alexander-Katz, A.; Ross, C. A.; Berggren, K. K. Templating Three-Dimensional Self-Assembled Structures in Bilayer Block Copolymer Films. *Science* **2012**, *336*, 1294–1298.
15. Jeong, S. J.; Kim, J. E.; Moon, H. S.; Kim, B. H.; Kim, S. M.; Kim, J. B.; Kim, S. O. Soft Graphoepitaxy of Block Copolymer Assembly with Disposable Photoresist Confinement. *Nano Lett.* **2009**, *9*, 2300–2305.
16. Cheng, J. Y.; Sanders, D. P.; Truong, H. D.; Harrer, S.; Friz, A.; Holmes, S.; Colburn, M.; Hinsberg, W. D. Simple and Versatile Methods To Integrate Directed Self-Assembly with Optical Lithography Using a Polarity-Switched Photoresist. *ACS Nano* **2010**, *4*, 4815–4823.
17. Bencher, C.; Smith, J.; Miao, L.; Cai, C.; Chen, Y.; Cheng, J. Y.; Sanders, D. P.; Tjio, M.; Truong, H. D.; Holmes, S.; Hinsberg, W. D. Self-assembly Patterning for Sub-15nm Half-pitch: A Transition from Lab to Fab. *Proc. SPIE* **2011**, *7970*, 79700F.
18. Liu, C.-C.; Pitera, J.; Lafferty, N.; Lai, K.; Rettner, C.; Tjio, M.; Arellano, N.; Cheng, J. Progress towards the Integration of Optical Proximity Correction and Directed Self-assembly of Block Copolymers with Graphoepitaxy. *Proc. SPIE* **2012**, *8323*, 83230X.
19. Takahashi, H.; Laachi, N.; Delaney, K. T.; Hur, S.-M.; Weinheimer, C. J.; Shykind, D.; Fredrickson, G. H. Defectivity in Laterally Confined Lamella-Forming Diblock Copolymers: Thermodynamic and Kinetic Aspects. *Macromolecules* **2012**, *45*, 6253–6265.
20. Patrone, P. N.; Gallatin, G. M. Modeling Line Edge Roughness in Templated, Lamellar Block Copolymer Systems. *Macromolecules* **2012**, *45*, 9507–9516.
21. Bang, J.; Kim, B. J.; Stein, G. E.; Russell, T. P.; Li, X.; Wang, J.; Kramer, E. J.; Hawker, C. J. Effect of Humidity on the Ordering of PEO-Based Copolymer Thin Films. *Macromolecules* **2007**, *40*, 7019–7025.

22. Park, W. I.; Kim, Y.; Jeong, J. W.; Kim, K.; Yoo, J.-K.; Hur, Y. H.; Kim, J. M.; Thomas, E. L.; Alexander-Katz, A.; Jung, Y. S. Host-Guest Self-assembly in Block Copolymer Blends. *Sci. Rep.* **2013**, *3*, 3190.
23. Jeong, J. W.; Hur, Y. H.; Kim, H.-j.; Kim, J. M.; Park, W. I.; Kim, M. J.; Kim, B. J.; Jung, Y. S. Proximity Injection of Plasticizing Molecules to Self-Assembling Polymers for Large-Area, Ultrafast Nanopatterning in the Sub-10-nm Regime. *ACS Nano* **2013**, *7*, 6747–6757.
24. Jeong, J. W.; Park, W. I.; Do, L.-M.; Park, J.-H.; Kim, T.-H.; Chae, G.; Jung, Y. S. Nanotransfer Printing with Sub-10 nm Resolution Realized using Directed Self-Assembly. *Adv. Mater.* **2012**, *24*, 3526–3531.
25. Lee, J.; Kim, K.; Park, W. I.; Kim, B.-H.; Park, J. H.; Kim, T.-H.; Bong, S.; Kim, C.-H.; Chae, G.; Jun, M.; Hwang, Y.; Jung, Y. S.; Jeon, S. Uniform Graphene Quantum Dots Patterned from Self-Assembled Silica Nanodots. *Nano Lett.* **2012**, *12*, 6078–6083.
26. Lodge, T. P.; Dalvi, M. C. Mechanisms of Chain Diffusion in Lamellar Block-Copolymers. *Phys. Rev. Lett.* **1995**, *75*, 657–660.
27. Jeong, J. W.; Park, W. I.; Kim, M.-J.; Ross, C. A.; Jung, Y. S. Highly Tunable Self-Assembled Nanostructures from a Poly(2-vinylpyridine-b-dimethylsiloxane) Block Copolymer. *Nano Lett.* **2011**, *11*, 4095–4101.
28. Kim, S. H.; Misner, M. J.; Xu, T.; Kimura, M.; Russell, T. P. Highly Oriented and Ordered Arrays from Block Copolymers *via* Solvent Evaporation. *Adv. Mater.* **2004**, *16*, 226–231.
29. Zhang, X.; Harris, K. D.; Wu, N. L.; Murphy, J. N.; Buriak, J. M. Fast Assembly of Ordered Block Copolymer Nanostructures through Microwave Annealing. *ACS Nano* **2010**, *4*, 7021–7029.
30. Park, W. I.; Kim, K.; Jang, H.-I.; Jeong, J. W.; Kim, J. M.; Choi, J.; Park, J. H.; Jung, Y. S. Directed Self-Assembly with Sub-100 Degrees Celsius Processing Temperature, Sub-10 Nanometer Resolution, and Sub-1 Minute Assembly Time. *Small* **2012**, *8*, 3762–3768.
31. Zhao, Y.; Sivaniah, E.; Hashimoto, T. SAXS Analysis of the Order−Disorder Transition and the Interaction Parameter of Polystyrene-Block-Poly(methyl methacrylate). *Macromolecules* **2008**, *41*, 9948–9951.
32. Barton, A. F. *CRC Handbook of Solubility Parameters and Other Cohesion Parameters*; CRC Press: Boca Raton, FL, 1991.
33. Gu, X.; Gunkel, I.; Hexemer, A.; Gu, W.; Russell, T. P. An *In Situ* Grazing Incidence X-Ray Scattering Study of Block Copolymer Thin Films During Solvent Vapor Annealing. *Adv. Mater.* **2014**, *26*, 273–281.
34. Hwa, S. C. P.; Ziegler, W. T. Temperature Dependence of Excess Thermodynamic Properties of Ethanol-Methylcyclohexane and Ethanol-Toluene Systems1. *J. Phys. Chem.* **1966**, *70*, 2572–2593.
35. Singh, A.; Mukherjee, M. Swelling Dynamics of Ultrathin Polymer Films. *Macromolecules* **2003**, *36*, 8728–8731.
36. Ruiz, R.; Bosworth, J. K.; Black, C. T. Effect of Structural Anisotropy on the Coarsening Kinetics of Diblock Copolymer Striped Patterns. *Phys. Rev. B: Condens. Matter Mater. Phys.* **2008**, *77*, 054204.
37. Xu, T.; Stevens, J.; Villa, J. A.; Goldbach, J. T.; Guarini, K. W.; Black, C. T.; Hawker, C. J.; Russell, T. P. Block Copolymer Surface Reconstuction: A Reversible Route to Nanoporous Films. *Adv. Funct. Mater.* **2003**, *13*, 698–702.
38. Cho, H.; Park, H.; Russell, T. P.; Park, S. Precise Placements of Metal Nanoparticles from Reversible Block Copolymer Nanostructures. *J. Mater. Chem.* **2010**, *20*, 5047–5051.